A&A, 703, A19 (2025)
https://doi.org/10.1051/0004-6361/202555392

Astronomy & Astrophysics

Unveiling blazar synchrotron emission: A multiwavelength polarimetric study of high-synchrotron and low-synchrotron peaked populations

Sara Capecchiacci[1,2,⋆], Ioannis Liodakis[1,3], Riccardo Middei[4,5,6], Dawoon E. Kim[7], Laura Di Gesu[8], Iván Agudo[9], Beatriz Agís-González[1], Axel Arbet-Engels[10], Dmitry Blinov[1,2], Chien-Ting Chen[11], Steven R. Ehlert[3], Ephraim Gau[12], Lea Heckmann[10,13], Kun Hu[12], Svetlana G. Jorstad[14,15], Philip Kaaret[3], Pouya M. Kouch[16,17], Henric Krawczynski[12], Elina Lindfors[16], Frédéric Marin[18], Alan P. Marscher[14], Ioannis Myserlis[19], Stephen L. O'Dell[3], Luigi Pacciani[7], David Paneque[10], Matteo Perri[5,4], Simonetta Puccetti[5], M. Lynne Saade[11,3], Fabrizio Tavecchio[20], Allyn F. Tennant[3], Efthalia Traianou[21,22], Martin C. Weisskopf[3], Kinwah Wu[23], Francisco José Aceituno[9], Giacomo Bonnoli[20,9], Víctor Casanova[9], Gabriel Emery[9], Juan Escudero[6,9], Daniel Morcuende[9], Jorge Otero-Santos[24,9], Alfredo Sota[9], Vilppu Piirola[18], George A. Borman[25], Evgenia N. Kopatskaya[15], Elena G. Larionova[15], Daria A. Morozova[15], Ekaterina V. Shishkina[15], Sergey S. Savchenko[15,26], Andrey A. Vasilyev[15], Tatiana S. Grishina[15], Ivan S. Troitskiy[15], Alexey V. Zhovtan[25], Callum McCall[27], Helen E. Jermak[27], Iain A. Steele[27], Rumen Bachev[28], Anton Strigachev[29], Ryo Imazawa[29], Mahito Sasada[30], Yasushi Fukazawa[29,31,32], Koji S. Kawabata[29,31,32], Makoto Uemura[29,31,32], Tsunefumi Mizuno[31], Tatsuya Nakaoka[31], Sumie Tochihara[29], Takahiro Akai[29], Hiroshi Akitaya[33], Andrei V. Berdyugin[16], Masato Kagitani[34], Vadim Kravtsov[16], Juri Poutanen[16], Takeshi Sakanoi[34], Diego Álvarez-Ortega[1,2], Carolina Casadio[1,2], Sincheol Kang[35], Sang-Sung Lee[35,36], Sanghyun Kim[35,36], Whee Yeon Cheong[35,36], Hyeon-Woo Jeong[35,36], Chanwoo Song[35,36], Shan Li[35,36], Myeong-Seok Nam[35,36], Mark Gurwell[6], Garrett Keating[6], Ramprasad Rao[6], Emmanouil Angelakis[37], Alexander Kraus[22], Petra Benke[38,22], Lena Debbrecht[22], Julia Eich[39], Florian Eppel[22,39], Andrea Gokus[12], Steven Hämmerich[40], Jonas Heßdörfer[22,39], Matthias Kadler[39], Dana Kirchner[39], Georgios Filippos Paraschos[22], Florian Rösch[22,39], and Wladislaw Schulga[39]

(Affiliations can be found after the references)

Received 5 May 2025 / Accepted 12 August 2025

ABSTRACT

The polarimetric properties of blazars enable us to place constraints on the acceleration mechanisms that fuel their powerful jets. By studying the multiwavelength polarimetric behaviour of high-synchrotron peaked (HSP) and low-synchrotron peaked (LSP) blazars, we aim to explore differences in their emission mechanisms and magnetic field structure in the acceleration region. In this study, we take advantage of several X-ray polarisation observations of HSP by the IXPE, including four new observations of Mrk 501, along with optical polarisation observations of LSP from RoboPol and other instruments. We find that the polarisation degree (PD) distribution of HSP in X-rays is systematically higher than in optical and mm-radio wavelengths, as reported in previous IXPE publications. The distribution of the X-ray electric vector position angles (PA) is centred around the jet axis with most of the observations consistent with zero difference within uncertainties. In fact, the distribution of the offset of the PA from the jet axis is consistent between the LSP and HSP populations (with PA measured in optical for the first, X-ray for the latter), suggesting a common magnetic field structure close to the acceleration region. These results offer strong support for the emerging energy stratified scenario of particle acceleration followed by energy loss in blazar jets.

Key words. techniques: polarimetric – Galaxy: nucleus – galaxies: active – BL Lacertae objects: general – galaxies: jets

1. Introduction

The jets of active galactic nuclei (AGN) are extremely luminous and their emission ranges from radio wavelengths up to the extremely energetic γ-rays. Their non-thermal radiation is commonly thought to arise from a highly collimated jet of particles accelerated to relativistic energies, extending along the polar axis of an accreting supermassive black hole (SMBH). In the specific case of blazars, the jet of magnetised plasma is oriented toward our line of sight. Their spectral energy distribution (SED) displays two humps, commonly known as the synchrotron and the high-energy hump. Based on the frequency of the synchrotron peak, we classify these sources into three classes: LSP sources (low-synchrotron peak), with $\nu_{\rm peak} < 10^{14}$ Hz; ISP sources (intermediate-synchrotron peak), with 10^{14} Hz $< \nu_{\rm peak} < 10^{15}$ Hz; and HSP sources (high-synchrotron peak), with $\nu_{\rm peak} > 10^{15}$ Hz. The acceleration mechanism of these particles is still unclear and under debate. The synchrotron hump arises from synchrotron radiation emitted by

⋆ Corresponding author.

accelerated electrons and positrons and peaks between infrared and X-rays. The high-energy (HE) component extends from the keV to the TeV energy range, and the responsible emission mechanism is commonly thought to be Compton scattering of photons by higher energy particles (Maraschi et al. 1992), but the origin of the seed photons is still unclear; some models also propose hadronic processes to contribute to the high-energy flux (Boettcher 2012).

There are still many open questions about blazars. For instance, the particle acceleration mechanism is still under debate. The primary theoretical models include moving or stationary shocks (i.e., plasma with a turbulent field crossing a shock front, Marscher & Gear 1985) and magnetic reconnection (Sironi et al. 2015). The magnetic field structure plays a pivotal role in particle acceleration and can be probed through multi-wavelength linear polarisation measurements. In the shock scenario, we expect particles to be accelerated in a small volume and lose energy while being advected away from the shock, encountering increasingly turbulent magnetic field areas, which would bring on a strongly chromatic PD (increasing with frequency). Due to the magnetic field of the plasma being parallel to the shock normal, the polarisation angle should be aligned with the jet direction (e.g., Hughes et al. 1985). In a magnetic reconnection scenario, we would expect lower polarisation degree (hereafter PD) for both optical and X-rays and random polarisation angles (hereafter PA), since the magnetic field is highly disordered (Bodo et al. 2021).

Optical polarisation observations using RoboPol (Ramaprakash et al. 2019) have reported that LSP sources in the optical range present stronger polarisation degrees, higher variability and large rotations of the polarisation angle compared to HSP; whereas HSP polarisation angles in the same range are more stable and exhibit a preferred direction (Blinov et al. 2016a; Angelakis et al. 2016). This can be explained by either shock acceleration or magnetic reconnection in a small volume close to the acceleration region: the highest energy particles (emitting at the synchrotron peak and beyond) are expected to be located in this small volume, losing energy as they move away from the acceleration region. Therefore, the highest polarisation degrees are expected close to the synchrotron peak due to the energy stratification, while the higher variability is related to smaller emission volumes. Smooth rotations of the polarisation angle are expected when plasma propagates through regions where the helical component of the magnetic field is dominant; further along the jet stream, the rotations are expected to be stochastic, due to the increase of turbulence in the magnetic field (Marscher 2014). If this is indeed a universal picture, we would expect to find a similar polarisation behaviour of HSP in the X-rays. Notably, the first observations of blazars in X-ray polarisation by the Imaging X-ray Polarimetry Explorer (IXPE, Weisskopf et al. 2022) have shown a chromatic polarisation degree with a polarisation angle roughly aligned with the jet axis (Liodakis et al. 2022; Di Gesu et al. 2022; Kouch et al. 2024), as well as smooth rotations of the polarisation angle (Di Gesu et al. 2023; Maksym et al. 2024)

We have now accumulated a sufficient number of IXPE HSP observations that can be used to more qualitatively probe whether the same characteristics (i.e., strong polarisation degrees and substantial rotations of the polarisation angle) can be found in LSP and HSP in the two different spectral ranges, corresponding to analogous regions of their spectral energy distributions. Here we aim to perform the first X-ray polarisation population study of blazars, exploring the similarities of HSP-X-ray to the LSP-optical polarisation for the first time. In Section 2, we present four new X-ray polarisation observations of Mrk 501 taken during IXPE Cycle 1. In Section 3, we present the HSP and LSP samples used in this work. The results of our population study are presented in Section 4. Our findings are discussed in Section 5.

2. New X-ray polarisation observations

IXPE is a joint NASA-ASI mission, launched on December 9, 2021. It is capable of measuring the degree of polarisation (PD) and the electric vector position angle (PA) in the 2–8 keV energy range. The analysis of the observations is generally performed using standard spectro-polarimetric analysis (Strohmayer 2017) through `XSPEC` (Arnaud 1996), with a log-parabola model (Massaro et al. 2004) used to fit the X-ray spectra, which represents the typical spectral shape of HSP both in quiescent and flaring states (Donnarumma et al. 2009; Baloković et al. 2016).

IXPE observed Mrk 501 four times during 2024 and 2025 (see Table B.2 for observation details). The first three observations resulted in a significant detection of the polarisation degree, whereas the fourth resulted in an upper limit (Fig. 1). For consistency, we followed the analysis given in previous IXPE-Mrk 501 papers (Liodakis et al. 2022; Chen et al. 2024). In line with previous observations, we found a variable polarisation degree between observations, with the polarisation angle aligned with the jet axis in all three cases (Fig. 2). We did not detect any polarisation variability within the 100 ksec IXPE exposures following the methodology described in Di Gesu et al. (2023) and Kim et al. (2024).

Simultaneously with the IXPE observations, several radio and optical telescopes have provided multiwavelength polarisation coverage. The multiwavelength data of the four new Mrk 501 observations are plotted in Fig. 1 (PD) and Fig. 2 (PA). The median of the radio and optical polarisation measurements can be found in Table B.2. In particular, these are the Belogradchik Observatory (Bachev 2024), Calar Alto Observatory (Agudo et al. 2012; Escudero Pedrosa et al. 2024), IRAM 30m Millimeter Radiotelescope through the POLAMI Program (Agudo et al. 2018), Effelsberg 100m telescope through the TELAMON (Eppel et al. 2024) and QUIVER (Kraus et al. 2003; Myserlis et al. 2018) programs, T60 at the Haleakala observatory (Piirola et al. 2014; Berdyugin et al. 2019; Piirola et al. 2021), Korean VLBI Network (KVN) array in single-dish mode (Kang et al. 2015), Nordic Optical Telescope (Nilsson et al. 2018), Liverpool Telescope (Jermak et al. 2018; Steele et al. 2004; Shrestha et al. 2020), LX-200, Submillimeter Array through the SMAPOL program (Myserlis et al., in prep.), Perkins Telescope (Jorstad & Marscher 2016), Sierra Nevada Observatory (Otero-Santos et al. 2024), and Skinakas observatory (Ramaprakash et al. 2019). The data analysis procedures and observing strategies are described in detail in Liodakis et al. (2022), Di Gesu et al. (2023), Peirson et al. (2023), Kouch et al. (2024, 2025). Polarisation measurements in the R band have been corrected for the host-galaxy contribution following Nilsson et al. (2007) and Hovatta et al. (2016). We note that Mrk 501 has shown consistent behaviour in all the X-ray polarisation observations so far, where all X-ray-optical-radio PA are aligned with the jet axis measured at 43 GHz, and the X-ray PD is typically more than two to three times higher than the optical PD and typically more than five to six times higher than the radio PD.

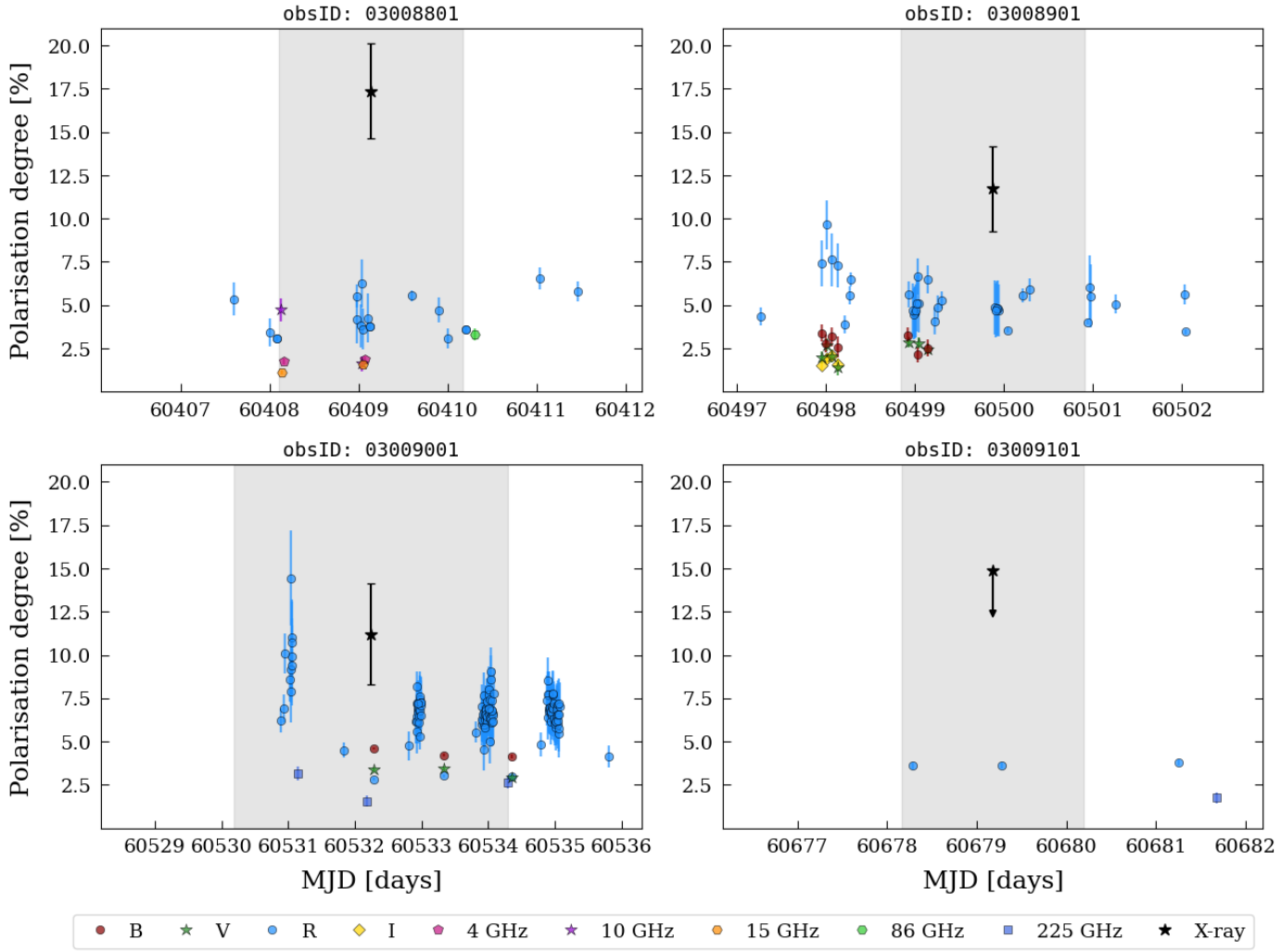

Fig. 1. Multiwavelength measurements of the PD of Mrk 501 simultaneous to the new IXPE observations. The IXPE observation times are highlighted in grey and its measurements are represented by the black stars.

3. Samples

This section aims to present the chosen sample for the LSP and HSP populations (i.e. ten sources and six sources, respectively). A detailed description of the sources taken into account and the observations used for this analysis can be found in Appendix A, namely, Table A.1. Specifically, a more detailed description of the HSP sample and the previous studies published by the IXPE collaboration can be found in Table A.2.

3.1. HSP sample

For the HSP sample, we used previously published multiwavelength polarisation data and jet directions for blazars (see Table A.2 for details), taken from previous works by the IXPE collaboration. Our sample consists of the following sources: 1ES 0229+200 (Ehlert et al. 2023), Mrk 421 (Di Gesu et al. 2022, 2023; Kim et al. 2024; Maksym et al. 2024), PG 1553+113 (Middei et al. 2023b), Mrk 501 (Chen et al. 2024; Liodakis et al. 2022), 1ES 1959+650 (Errando et al. 2024; Pacciani et al. 2025), and PKS 2155−304 (Kouch et al. 2024), in order of increasing right ascension (RA).

We only consider strictly simultaneous observations in the optical and mm-radio bands. For some observations of Mrk 421 and 1ES 1959+650, we used time-resolved results of the polarisation analysis, instead of the average values (this was done for observations from Di Gesu et al. 2023 and Maksym et al. 2024, as well as for the second observation from Errando et al. 2024). In particular, for 1ES 1959+650 we only use one of the four time bins reported by the authors, as the other three are upper limits. These sources are the only two in the sample presenting large deviations of the PA from the jet angle.

We filtered the data by selecting only 3σ detections ($PD_{value}/PD_{error} > 3$). For the optical observations, we considered the R band measurements since it is the only optical band corrected for the host galaxy contribution. For the mm-radio observations, we used the highest available frequency, typically 225 GHz.

3.2. LSP sample

We began our sample selection from the RoboPol monitoring program (Blinov et al. 2021), which includes observations of 222 AGN at Dec. $>-25°$ from 2013 to 2017 in the R band; however, only a small subset of 61 sources was monitored regularly. We selected all LSP sources (Ajello et al. 2020) with available jet directions from Weaver et al. (2022). Our final sample consists of the common ten sources, namely PKS 0420−01,

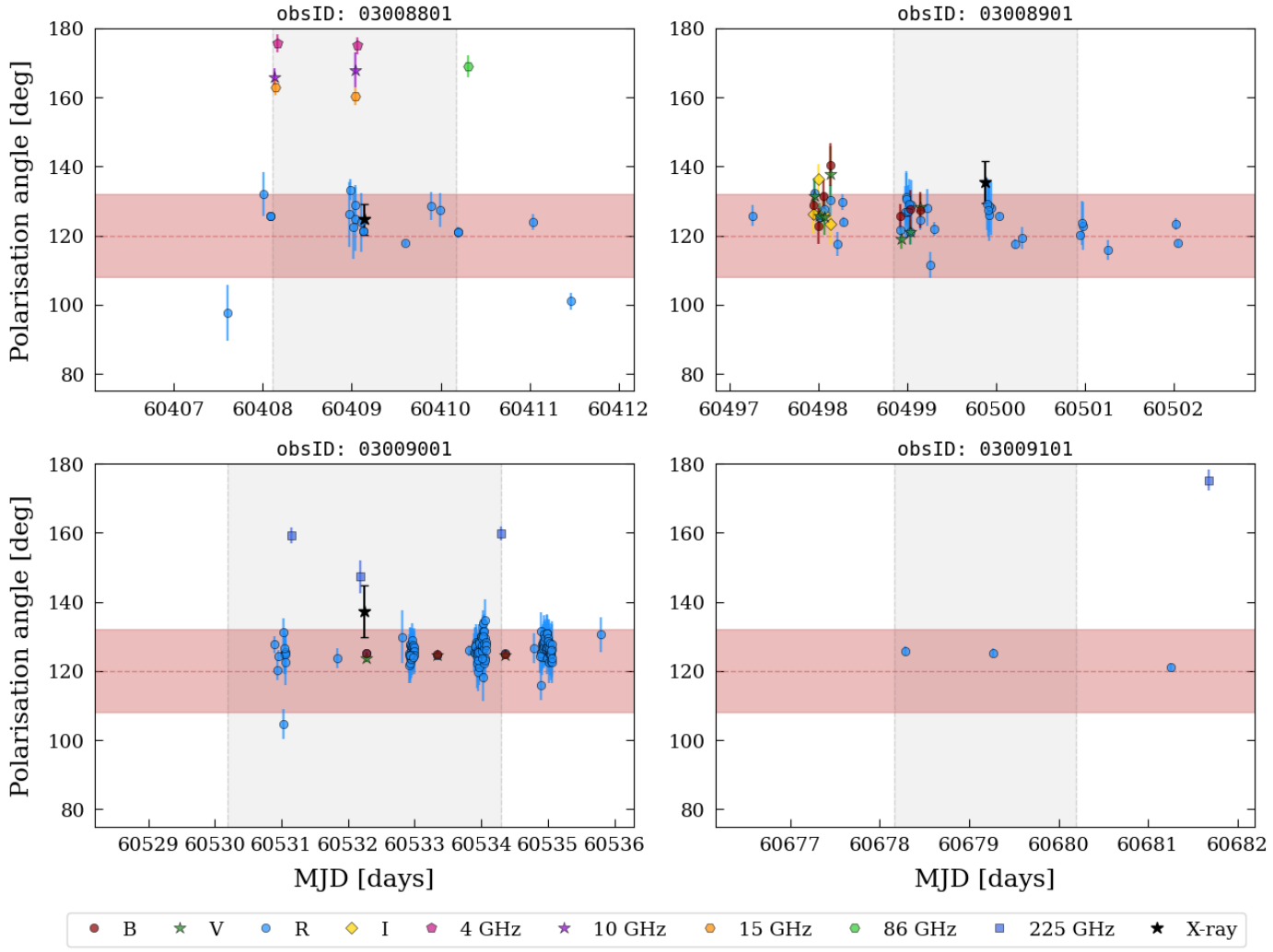

Fig. 2. Multiwavelength measurements of the PA of Mrk 501 simultaneous to the new IXPE observations. The IXPE observation times are highlighted in grey and its measurements are represented by the black stars. The jet direction is represented by the red dashed line, with its uncertainty represented by the red shaded area. The fourth panel is missing the X-ray PA measurement, as the IXPE PD measurement is a 3σ upper limit and therefore the polarisation angle is not defined.

4C 71.07, PKS 1510−089, 4C 38.41, 3C 345, 4C 09.57, BL Lac, 3C 446, 4C 11.69, and 3C 454.3, in order of increasing RA. For 3C 454.3 and BL Lac, we included additional optical polarisation observations from the IXPE campaigns (Middei et al. 2023a; Peirson et al. 2023; Marshall et al. 2024; Agudo et al. 2025).

The initial sample also included 3C 273; however, this source was removed from this study, as its strong accretion disk contribution to the optical emission might have lowered the overall polarisation degree.

4. Population analysis

4.1. X-ray polarisation analysis

Using the simultaneous multiwavelength HSP observations we plot the distribution of the X-ray, optical and radio polarisation degree (Fig. 3) and their ratios (Fig. 4). We note that these figures represent all of the observations taken into account for the six HSP sources in our sample: separate observations of the same source sample the same underlying magnetic field structure and particle acceleration properties of that object. The different observations are shown for completeness, but the median values of the polarisation properties as likely more representative. The median values of PD and PA for each source can be found in Table A.1. As noted in previous publications discussing IXPE observations, the X-ray PD is consistently higher than the optical, which in turn is higher than the radio, in line with the energy stratification of the emission owing to particle cooling. The median X-ray to optical ratio of our HSP sample is 2.5, with a standard deviation of 2.0; the median X-ray to radio ratio is 6.0, with a standard deviation of 2.5; the median optical to radio ratio is 1.7, with a standard deviation of 0.7. We note that radio measurements were not available for every IXPE observation interval, so the number of radio observations included in the analysis is lower than the number of optical and X-ray observations.

We also explored the difference between the measured PA and the jet direction in the X-ray range for every observation. This is particularly important because different acceleration mechanisms correspond to different angles between the magnetic field and the jet axis. The results are shown in Figure 5. The X-ray PA offset from the jet axis is centred around zero with a median of 2.5° and a standard deviation of 17.5° (due to the two sources that present large departures of the PA from the jet). This

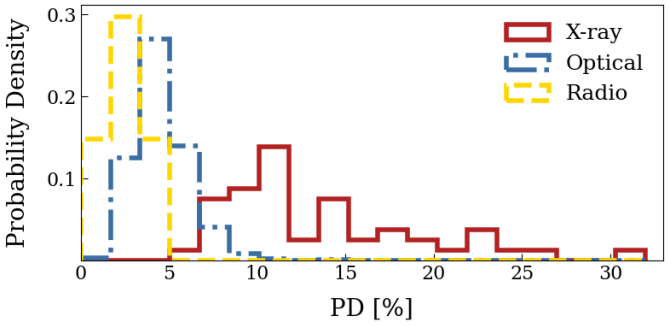

Fig. 3. Measured PD of all HSP observations in each spectral range: X-ray (red solid line), optical (blue dash-dotted line), and mm-radio (yellow dashed line). The histogram is normalised due to the low number of radio observations with respect to the other bands.

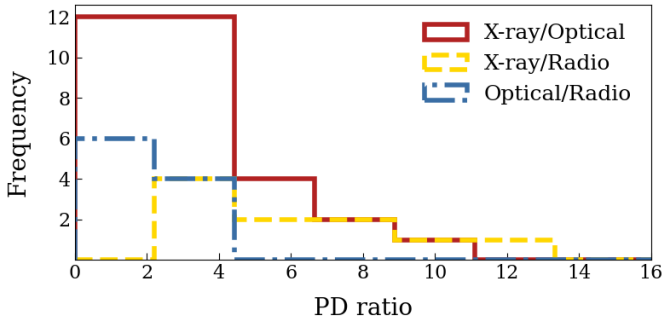

Fig. 4. Ratio of HSP PD between the different ranges, computed for all HSP observations: X-ray over optical (red solid line), X-ray over mm-radio (yellow dashed line), and optical over mm-radio (blue dash-dotted line).

would suggest that during quiescent or average states, the X-ray PA in HSP fluctuates about the jet axis. Large deviations (>50°) from the jet axis alignment are observed only for Mrk 421, during rotations of the polarisation angle, and for 1ES 1959+650 (plotted separately in Fig. 5). We note that this figure also reports all observations separately to underline the wide range of PA values measured for each source. This is similar to the optical polarisation behaviour observed in LSP during PA rotations and it is often attributed to the emergence of new polarisation components crossing the radio core (Liodakis et al. 2020; Kouch et al. 2025).

4.2. HSP-X-ray compared to LSP-optical

We then proceeded with a comparison between the HSP sample and the LSP sample. The analysis focuses on two different wavelength ranges (X-rays for HSP and optical for LSP), as these correspond to analogous regions of their spectral energy distributions. The PD distributions of the two samples are shown in Figure 6a. The median HSP PD is 11.4%, with standard deviation 5.1%, while for LSP it is 5.8%, with a standard deviation of 4.0%. The HSP generally show higher PD than the LSP (confirmed by the Wilcox test applied on the two distributions); however, this may be attributed to an observational bias at X-ray wavelengths: the combination of the typical IXPE exposure of 100 ksec and the typical HSP flux ($\approx 10^{-10}$ erg s^{-1} cm^{-2}) yields a minimum detectable polarisation degree at the 99% confidence interval (MDP$_{99}$, Weisskopf et al. 2010) of about 5–6%. Since lower values cannot be measured (and indeed we have omitted upper limits for Mrk 501 and 1ES 1959+650), the X-ray PD

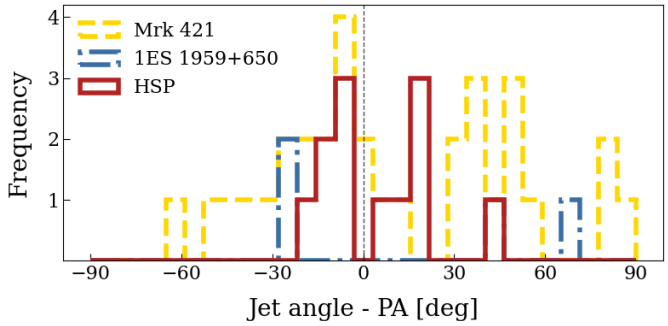

Fig. 5. Histogram of the angular difference between the jet and the X-ray PA, computed for every HSP observation. Mrk 421 (yellow dashed line) and 1ES 1959+650 (blue dash-dotted line) are plotted separately from the others, as they present large amplitude rotations of the PA during the IXPE observation periods. The other sources are plotted altogether (red solid line).

distribution is skewed to higher values. The disk emission can also lower the optical PD of LSP, as it is unpolarised and strong in the optical range (but not in the X-rays and, thus, not for HSP).

We also repeated the analysis of the PA offset from the jet described in the previous section for the LSP sample. Both HSP and LSP distributions are shown in Figs. 6b and 7. We found similar results for the LSP, with a median of 15.87% and a standard deviation of 27.1%. To compare the distributions of PD and of PA alignment of the two samples, we applied the Anderson-Darling test (hereafter A-D). The A-D is a non-parametric test to assess whether the observations come from the same parent population (Anderson & Darling 1952). We set a p-value threshold to reject the null hypothesis, stating that the two distributions come from the same parent distribution, at 0.05. We applied the test on the distributions of median PD and of median PA offset from the jet direction. The test results are reported in Table 1. We also compared the LSP sample to the HSP sample excluding Mrk 421, to assess whether the much larger number of Mrk 421 observatons (compared to other HSP) has an effect on our comparison. Considering the whole HSP sample, we found consistency among the PA offset distributions, along with a mild inconsistency among the PD distributions. Excluding Mrk 421 does not alter the results for the PA offset, but yields a result of consistency for the PD distributions. Our results on the PA analysis point towards the possibility of a similar magnetic field configuration in the acceleration region for HSP and LSP. The results of these comparisons are discussed in detail in the next section.

Finally, we searched for similarities in the behaviour of the Compton dominance of LSP and HSP. This quantity is defined as the ratio between the energy flux per logarithmic interval of frequency: $\nu F_{\nu,HE}$ at the high-energy peak frequency and $\nu F_{\nu,syn}$ at the synchrotron peak frequency. It can help indicate the dominant process in the high-energy emission. HSP sources typically have Compton dominance values lower than one, while LSP can greatly exceed unity. We use the values listed in the Fermi 4LAC catalog (Ajello et al. 2020) to compute the Compton dominance for each source and plot it against the median X-ray PD in the case of HSP and the median optical PD for LSP (Fig. 8). We note that the Compton dominance values are calculated from the synchrotron and high-energy peak fluxes averaged over the decades of observations. Nevertheless, our results highlight an anticorrelation between the Compton dominance and the polarisation degree, along with a fairly good consistency between the HSP and LSP samples.

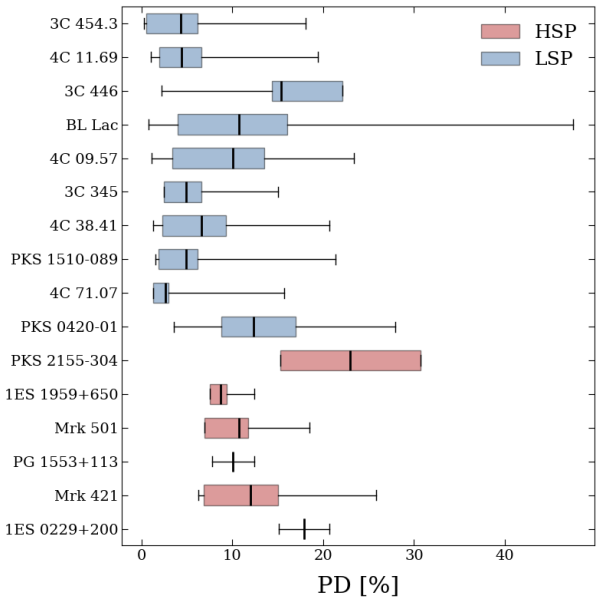

(a)

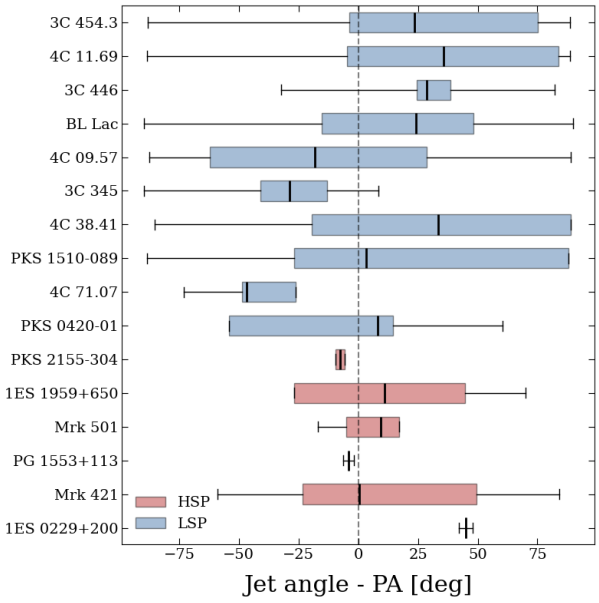

(b)

Fig. 6. PD of the sources in our sample represented in the first box plot (LSP in blue, above; HSP in red, below). The angular difference between the jet direction and the PA of the sources is represented in the second box plot, with the dashed black line indicating a difference of 0° (LSP in blue, above; HSP in red, below). The black vertical line inside the coloured box marks the median over all observations. The coloured box represents the shortest interval containing 68% of the observations, while the horizontal black lines extend to the full range of values measured across all observations considered. Note: for PKS 2155−304 the coloured box covers the full range, as we only had two observations; for PG 1553+113 and 1ES 0229+200, we only had one observation, so we represent the measurement and its error.

5. Discussion

Figure 3, representing all observations taken into account for this work, highlights that the mm-radio PD is generally lower than the optical PD, which, in turn, is generally lower than

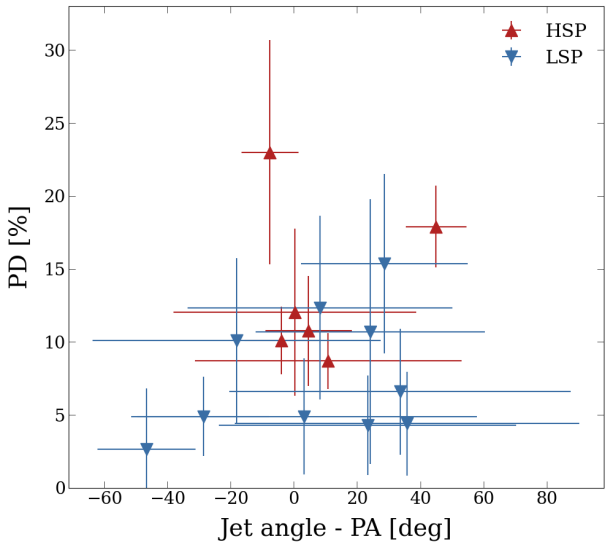

Fig. 7. Median PA offset from the jet plotted versus the median PD of each object (in X-rays for HSP, red upward triangles; in optical for LSP, blue downward triangles). Note: the median values are the most crucial for this study, as they represent the average behaviour of an object.

Table 1. *P*-values resulting from the A-D test applied to the HSP and LSP median PD distributions, and to the distributions of the median difference PA-jet direction.

Distribution	*p*-value
PD	0.043
PA offset	0.250

(a) LSP sample compared to the whole HSP sample.

Distribution	*p*-value
PD	0.056
PA offset	0.250

(b) LSP sample compared to HSP sample excluding Mrk 421.

the X-ray PD. In fact, a similar behaviour had previously been observed in BL Lacertae (LSP/ISP source) during a flaring state (Peirson et al. 2023) in which the high-energy tail of the synchrotron emission was detected by IXPE. Similarly to HSP, BL Lacertae showed a higher X-ray PD than optical and mm-radio, with the PA aligned with the jet axis within uncertainties. The overall observed multiwavelength polarisation behaviour is naturally explained by shock acceleration, which starts with a well-ordered magnetic field within the acceleration region, growing progressively more turbulent further downstream, resulting in a decreasing PD with longer wavelengths (Liodakis et al. 2022). However, the dominant underlying process driving the decrease in PD is particle cooling and advection from the acceleration region, which can also occur under alternative acceleration scenarios. In the absence of alternative scenario simulations demonstrating a chromatic PD, we still favour shocks as the dominant acceleration mechanism, which is also supported by shock acceleration simulations (Tavecchio et al. 2018; Sciaccaluga et al. 2025).

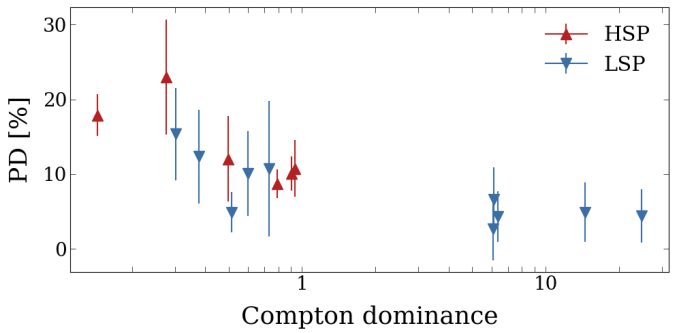

Fig. 8. Compton dominance of the sources (logarithmic scale) plotted against their median PD (in the X-rays for HSP, red upward triangles, and optical for LSP, blue downward triangles).

Recently, an alternative model was proposed by Bolis et al. (2024), which looks for a similar solution through confined, magnetically dominated jets, where the polarisation strongly depends on the magnetic field configuration. Under this scenario, our observations would suggest that the jet is nearly parabolic in the acceleration region. This is, in fact, supported by VLBI observations of blazars and nearby radio galaxies (Kovalev et al. 2020).

As for the comparison between HSP and LSP, we did find mild inconsistencies between the PD distributions of the two populations, which do not appear to be drawn from the same parent population, according to the resulting p-value.

The offset between the PA and the jet direction is centered around zero for both HSP (median 2.5°, standard deviation 17.5°) and LSP (median 15.8°, standard deviation 27.1°), with the A-D test suggesting that we cannot reject the hypothesis that both distributions come from the same parent population. Over a total number of 2247 LSP observations, 876 (≈39%) present a PA offset consistent with 0 within 3σ; for HSP, over a total of 48 data points, 30 (≈63%) do. For each comparison, we applied the test on the distribution of median values, as the median represents the average behaviour of the source. Our results suggest that the magnetic field configuration in the acceleration region is the same for HSP and LSP, providing strong evidence to support the energy-stratified picture.

Previous studies have shown that during flaring states, the variability of the polarisation properties can be associated with moving components within the jet, which result in rotations of the PA (Marscher et al. 2008; Marscher & Jorstad 2010). There are several notable examples in optical polarisation for LSP (Liodakis et al. 2020; Kouch et al. 2025) and possibly in X-ray polarisation for HSP (Kim et al. 2024), further supporting this picture.

Blinov et al. (2016a) demonstrated that not all blazars show rotations of the optical PA; rather, it is a smaller sample that is predominantly LSP. Specifically, only 13 out of 33 LSP (39%) in the monitored RoboPol sample showed rotations during the three-year program. Of the six HSP observed by IXPE, only Mrk 421 and 1ES 1959+650 show large rotations (33%). Given the similarity of the LSP-optical to the HSP-X-ray polarisation found in this work, it is not unreasonable to expect only two sources to exhibit rotations. More IXPE observations of alternative HSP sources will provide the opportunity to discover more rotations of the PA and constrain their origin. Interestingly, PG 1553+113 has been shown to exhibit optical rotations (Blinov et al. 2016a, 2018; Middei et al. 2023b), making it a prime candidate for detecting X-ray PA rotations. The rotations observed in the optical range for the LSP were often associated with γ-ray flares (Blinov et al. 2016b, 2018). It is then reasonable to expect that the observed X-ray PA rotations in HSP may be associated to VHE γ-ray flares, as previously observed in Mrk 421 (MAGIC Collaboration 2025). This highlights the promising synergy between IXPE and upcoming TeV facilities such as CTA (Zanin et al. 2022).

For both HSP and LSP, we found a general decrease in the polarisation degree with the increasing Compton dominance. Of the five LSP sources presenting a Compton dominance lower than 1, two are classified as BL Lac objects and three as flat-spectrum radio quasars (Ajello et al. 2020). The strong anticorrelation between PD and Compton dominance is confirmed by the Spearman test, which yields a p-value of 0.00004 and a correlation coefficient r of −0.84. This anticorrelation can be interpreted as due to the increasing contribution of the high-energy component of the SED to the observed bands. The observed high-energy side of the synchrotron spectrum is in reality the superposition of both synchrotron and high-energy hump emission: while the synchrotron emission is polarised, the low-energy side of the high-energy emission component is likely dominated by the less polarised Compton scattering emission (Agudo et al. 2025; Liodakis et al. 2025). As the contribution of the Compton emission becomes dominant over the total emission, the overall PD is lowered. To confirm or discard this hypothesis, a more thorough study of this relation considering simultaneous data is necessary.

6. Conclusions

In this work, we compare two blazar populations consisting of LSP and HSP, looking for similarities in their polarisation properties, particularly in the PD, as well as the difference between the jet direction and the PA.

The main results of this study can be summarised below.

- Four new IXPE observations of Mrk 501 support earlier reports of the X-ray PD generally being more than two to three times larger than the optical and more than five to six times larger than the millimetre radio.
- The HSP population shows chromaticity, where the PD increases with increasing frequency (Figure 3). The median of the X-ray to optical and X-ray to radio PD ratios are 2.5 and 6.0, respectively. This supports the energy stratified picture where particles are accelerated and then advected from the acceleration region as they cool down (Liodakis et al. 2022).
- The X-ray PA are typically aligned with the jet axis, except during large rotations of the polarisation angle (as observed in Mrk 421). Combined with the chromaticity of the PD, this provides further evidence of shock acceleration in blazar jets.
- The optical PA of LSP and the X-ray PA of HSP show consistent behaviour, possibly suggesting a common energy-stratification scenario for blazar jets, as predicted in Angelakis et al. (2016). The detection of X-ray PA rotations in Mrk 421 and 1ES 1959+650 further confirms this hypothesis, suggesting that some HSP can show X-ray PA rotations, although not all HSP will, similarly to previous results for LSP rotations in the optical range (Blinov et al. 2016a). Access to more HSP observations could be beneficial to detecting additional X-ray rotations, with PG 1553+113 a likely prime candidate.
- The PD of both LSP and HSP decreases with increasing Compton dominance. This is consistent with the hypothesis of a superposition of synchrotron and Compton emission,

with the first being polarised and the latter unpolarised. A more thorough study of this relation should be performed by considering the simultaneous SED, rather than the long-term averages considered here.

Acknowledgements. This research has made use of data from the RoboPol programme, a collaboration between Caltech, the University of Crete, IA-FORTH, IUCAA, the MPIfR, and the Nicolaus Copernicus University, which was conducted at Skinakas Observatory in Crete, Greece. The Imaging X-ray Polarimetry Explorer (IXPE) is a joint US and Italian mission. The US contribution is supported by the National Aeronautics and Space Administration (NASA) and led and managed by its Marshall Space Flight Center (MSFC), with industry partner Ball Aerospace (now, BAE Systems). The Italian contribution is supported by the Italian Space Agency (Agenzia Spaziale Italiana, ASI) through contract ASI-OHBI-2022-13-I.0, agreements ASI-INAF-2022-19-HH.0 and ASI-INFN-2017.13-H0, and its Space Science Data Center (SSDC) with agreements ASI-INAF-2022-14-HH.0 and ASI-INFN 2021-43-HH.0, and by the Istituto Nazionale di Astrofisica (INAF) and the Istituto Nazionale di Fisica Nucleare (INFN) in Italy. This research used data products provided by the *IXPE* Team (MSFC, SSDC, INAF, and INFN) and distributed with additional software tools by the High-Energy Astrophysics Science Archive Research Center (HEASARC), at NASA Goddard Space Flight Center (GSFC). The IAA-CSIC co-authors acknowledge financial support from the Spanish "Ministerio de Ciencia e Innovación" (MCIN/AEI/ 10.13039/501100011033) through the Center of Excellence Severo Ochoa award for the Instituto de Astrofísica de Andalucía-CSIC (CEX2021-001131-S), and through grants PID2019-107847RB-C44 and PID2022-139117NB-C44. Some of the data are based on observations collected at the Observatorio de Sierra Nevada; which is owned and operated by the Instituto de Astrofísica de Andalucía (IAA-CSIC), and at the Centro Astronómico Hispano en Andalucía (CAHA); which is operated jointly by Junta de Andalucía and Consejo Superior de Investigaciones Científicas (IAA-CSIC). The POLAMI observations reported here were carried out at the IRAM 30m Telescope. IRAM is supported by INSU/CNRS (France), MPG (Germany) and IGN (Spain). The Submillimeter Array is a joint project between the Smithsonian Astrophysical Observatory and the Academia Sinica Institute of Astronomy and Astrophysics and is funded by the Smithsonian Institution and the Academia Sinica. Maunakea, the location of the SMA, is a culturally important site for the indigenous Hawaiian people; we are privileged to study the cosmos from its summit. E.L. was supported by Academy of Finland projects 317636 and 320045. The research at Boston University was supported in part by National Science Foundation grant AST-2108622, NASA Fermi Guest Investigator grant 80NSSC23K1507, NASA *NuSTAR* Guest Investigator grant 80NSSC24K0565, and NASA Swift Guest Investigator grant 80NSSC23K1145. The Perkins Telescope Observatory, located in Flagstaff, AZ, USA, is owned and operated by Boston University. This work was supported by NSF grant AST-2109127. This work was supported by JST, the establishment of university fellowships towards the creation of science technology innovation, Grant Number JPMJFS2129. This work was supported by Japan Society for the Promotion of Science (JSPS) KAKENHI Grant Numbers JP21H01137. This work was also partially supported by Optical and Near-Infrared Astronomy Inter-University Cooperation Program from the Ministry of Education, Culture, Sports, Science and Technology (MEXT) of Japan. We are grateful to the observation and operating members of Kanata Telescope. S. Kang, S.-S. Lee, W. Y. Cheong, S.-H. Kim, H.-W. Jeong, C. Song, S. Li, and M.-S. Nam were supported by the National Research Foundation of Korea (NRF) grant funded by the Korea government (MIST) (2020R1A2C2009003, RS-2025-00562700). The KVN is a facility operated by the Korea Astronomy and Space Science Institute. The KVN operations are supported by KREONET (Korea Research Environment Open NETwork) which is managed and operated by KISTI (Korea Institute of Science and Technology Information). S. C., B. A-G., and I. L. were funded by the European Union ERC-2022-STG – BOOTES – 101076343. Views and opinions expressed are however those of the author(s) only and do not necessarily reflect those of the European Union or the European Research Council Executive Agency. Neither the European Union nor the granting authority can be held responsible for them. The data in this study include observations made with the Nordic Optical Telescope, owned in collaboration by the University of Turku and Aarhus University, and operated jointly by Aarhus University, the University of Turku and the University of Oslo, representing Denmark, Finland and Norway, the University of Iceland and Stockholm University at the Observatorio del Roque de los Muchachos, La Palma, Spain, of the Instituto de Astrofisica de Canarias. The data presented here were obtained in part with ALFOSC, which is provided by the Instituto de Astrofísica de Andalucía (IAA) under a joint agreement with the University of Copenhagen and NOT. We acknowledge funding to support our NOT observations from the Finnish Centre for Astronomy with ESO (FINCA), University of Turku, Finland (Academy of Finland grant nr 306531). This research was partially supported by the Bulgarian National Science Fund of the Ministry of Education and Science under grants KP-06-H68/4 (2022), KP-06-H78/5 (2023) and KP-06-H88/4 (2024). The Liverpool Telescope is operated on the island of La Palma by Liverpool John Moores University in the Spanish Observatorio del Roque de los Muchachos of the Instituto de Astrofisica de Canarias with financial support from the UKRI Science and Technology Facilities Council (STFC) (ST/T00147X/1). Partly based on observations with the 100-m telescope of the MPIfR (Max-Planck-Institut für Radioastronomie) at Effelsberg. Observations with the 100-m radio telescope at Effelsberg have received funding from the European Union's Horizon 2020 research and innovation programme under grant agreement No 101004719 (ORP). F.E., S.H., J.H., M.K., and F.R. acknowledge support from the Deutsche Forschungsgemeinschaft (DFG, grants 447572188, 434448349, 465409577). G. F. P. acknowledges support by the European Research Council advanced grant "M2FINDERS – Mapping Magnetic Fields with INterferometry Down to Event hoRizon Scales" (Grant No. 101018682). C.C., D.B. and D.A. acknowledge support from the European Research Council (ERC) under the Horizon ERC Grants 2021 programme under grant agreement No. 101040021. P.K. was supported by Academy of Finland projects 346071 and 345899. P.K. acknowledges support from the Metsähovi Radio Observatory of Aalto University. J.O.-S. acknowledges founding from the Istituto Nazionale di Fisica Nucleare Cap. U.1.01.01.01.009.

References

Agudo, I., Liodakis, I., Otero-Santos, J., et al. 2025, ApJ, 985, L15
Agudo, I., Molina, S. N., Gómez, J. L., et al. 2012, Int. J. Mod. Phys. Conf. Ser., 8, 299
Agudo, I., Thum, C., Molina, S. N., et al. 2018, MNRAS, 474, 1427
Ajello, M., Angioni, R., Axelsson, M., et al. 2020, ApJ, 892, 105
Anderson, T. W., & Darling, D. A. 1952, Ann. Math. Stat., 193
Angelakis, E., Hovatta, T., Blinov, D., et al. 2016, MNRAS, 463, 3365
Arnaud, K. A. 1996, in Astronomical Data Analysis Software and Systems V, eds. G. H. Jacoby, & J. Barnes, ASP Conf. Ser., 101, 17
Bachev, R. 2024, Bulg. Astron. J., 40, 78
Baloković, M., Paneque, D., Madejski, G., et al. 2016, ApJ, 819, 156
Berdyugin, A., Piirola, V., & Poutanen, J. 2019, in Astronomical Polarisation from the Infrared to Gamma Rays, eds. R. Mignani, A. Shearer, A. Słowikowska, & S. Zane, Astrophysics and Space Science Library, 460, 33
Blinov, D., Pavlidou, V., Papadakis, I., et al. 2016a, MNRAS, 462, 1775
Blinov, D., Pavlidou, V., Papadakis, I. E., et al. 2016b, MNRAS, 457, 2252
Blinov, D., Pavlidou, V., Papadakis, I., et al. 2018, MNRAS, 474, 1296
Blinov, D., Kiehlmann, S., Pavlidou, V., et al. 2021, MNRAS, 501, 3715
Bodo, G., Tavecchio, F., & Sironi, L. 2021, MNRAS, 501, 2836
Boettcher, M. 2012, ArXiv e-prints [arXiv:1205.0539]
Bolis, F., Sobacchi, E., & Tavecchio, F. 2024, Phys. Rev. D, 110, 123032
Chen, C.-T. J., Liodakis, I., Middei, R., et al. 2024, ApJ, 974, 50
Di Gesu, L., Donnarumma, I., Tavecchio, F., et al. 2022, ApJ, 938, L7
Di Gesu, L., Marshall, H. L., Ehlert, S. R., et al. 2023, Nat. Astron., 7, 1245
Donnarumma, I., Vittorini, V., Vercellone, S., et al. 2009, ApJ, 691, L13
Ehlert, S. R., Liodakis, I., Middei, R., et al. 2023, ApJ, 959, 61
Eppel, F., Kadler, M., Heßdörfer, J., et al. 2024, A&A, 684, A11
Errando, M., Liodakis, I., Marscher, A. P., et al. 2024, ApJ, 963, 5
Escudero Pedrosa, J., Agudo, I., Morcuende, D., et al. 2024, AJ, 168, 84
Hovatta, T., Lindfors, E., Blinov, D., et al. 2016, A&A, 596, A78
Hughes, P. A., Aller, H. D., & Aller, M. F. 1985, ApJ, 298, 301
Jermak, H., Steele, I. A., & Smith, R. J. 2018, in Ground-based and Airborne Instrumentation for Astronomy VII, eds. C. J. Evans, L. Simard, & H. Takami, SPIE Conf. Ser., 10702, 107024Q
Jorstad, S., & Marscher, A. 2016, Galaxies, 4, 47
Kang, S., Lee, S.-S., & Byun, D.-Y. 2015, J. Korean Astron. Soc., 48, 257
Kim, D. E., Di Gesu, L., Liodakis, I., et al. 2024, A&A, 681, A12
Kouch, P. M., Liodakis, I., Middei, R., et al. 2024, A&A, 689, A119
Kouch, P. M., Liodakis, I., Fenu, F., et al. 2025, A&A, 695, A99
Kovalev, Y. Y., Pushkarev, A. B., Nokhrina, E. E., et al. 2020, MNRAS, 495, 3576
Kraus, A., Krichbaum, T. P., Wegner, R., et al. 2003, A&A, 401, 161
Liodakis, I., Blinov, D., Jorstad, S. G., et al. 2020, ApJ, 902, 61
Liodakis, I., Marscher, A. P., Agudo, I., et al. 2022, Nature, 611, 677
Liodakis, I., Zhang, H., Boula, S., et al. 2025, A&A, 698, L19
MAGIC Collaboration (Abe, K., et al.) 2025, A&A, 695, A217
Maksym, W. P., Liodakis, I., Saade, M. L., et al. 2024, ArXiv e-prints [arXiv:2410.19983]
Maraschi, L., Ghisellini, G., & Celotti, A. 1992, ApJ, 397, L5
Marscher, A. P. 2014, ApJ, 780, 87
Marscher, A. P., & Gear, W. K. 1985, ApJ, 298, 114
Marscher, A. P., & Jorstad, S. G. 2010, ArXiv e-prints [arXiv:1005.5551]
Marscher, A. P., Jorstad, S. G., D'Arcangelo, F. D., et al. 2008, Nature, 452, 966
Marshall, H. L., Liodakis, I., Marscher, A. P., et al. 2024, ApJ, 972, 74

Massaro, E., Perri, M., Giommi, P., & Nesci, R. 2004, A&A, 413, 489
Middei, R., Liodakis, I., Perri, M., et al. 2023a, ApJ, 942, L10
Middei, R., Perri, M., Puccetti, S., et al. 2023b, ApJ, 953, L28
Myserlis, I., Angelakis, E., Kraus, A., et al. 2018, A&A, 609, A68
Nilsson, K., Pasanen, M., Takalo, L. O., et al. 2007, A&A, 475, 199
Nilsson, K., Lindfors, E., Takalo, L. O., et al. 2018, A&A, 620, A185
Otero-Santos, J., Piirola, V., Escudero Pedrosa, J., et al. 2024, AJ, 167, 137
Pacciani, L., Kim, D. E., Middei, R., et al. 2025, ApJ, 983, 78
Peirson, A. L., Negro, M., Liodakis, I., et al. 2023, ApJ, 948, L25
Piirola, V., Berdyugin, A., & Berdyugina, S. 2014, in Ground-based and Airborne Instrumentation for Astronomy V, eds. S. K. Ramsay, I. S. McLean, & H. Takami, SPIE Conf. Ser., 9147, 91478I
Piirola, V., Kosenkov, I. A., Berdyugin, A. V., Berdyugina, S. V., & Poutanen, J. 2021, AJ, 161, 20
Piner, B. G., & Edwards, P. G. 2018, ApJ, 853, 68
Ramaprakash, A. N., Rajarshi, C. V., Das, H. K., et al. 2019, MNRAS, 485, 2355
Sciaccaluga, A., Costa, A., Tavecchio, F., et al. 2025, A&A, 699, A296
Shrestha, M., Melandri, A., Smith, R., et al. 2020, GRB Coordinates Network, 29085, 1
Sironi, L., Petropoulou, M., & Giannios, D. 2015, MNRAS, 450, 183
Steele, I. A., Smith, R. J., Rees, P. C., et al. 2004, in Ground-based Telescopes, ed. J. M. Oschmann, Jr., SPIE Conf. Ser., 5489, 679
Strohmayer, T. E. 2017, ApJ, 838, 72
Tavecchio, F., Landoni, M., Sironi, L., & Coppi, P. 2018, MNRAS, 480, 2872
Weaver, Z. R., Jorstad, S. G., Marscher, A. P., et al. 2022, ApJS, 260, 12
Weisskopf, M. C., Elsner, R. F., & O'Dell, S. L. 2010, in Space Telescopes and Instrumentation 2010: Ultraviolet to Gamma Ray, eds. M. Arnaud, S. S. Murray, & T. Takahashi, SPIE Conf. Ser., 7732, 77320E
Weisskopf, M. C., Soffitta, P., Baldini, L., et al. 2022, J. Astron. Telesc. Instrum. Syst., 8, 026002
Zanin, R., Abdalla, H., Abe, H., et al. 2022, 37th International Cosmic Ray Conference, 5

[1] Institute of Astrophysics, Foundation for Research and Technology-Hellas, GR-71110 Heraklion, Greece
[2] Department of Physics, University of Crete, 70013, Heraklion, Greece
[3] NASA Marshall Space Flight Center, Huntsville, AL 35812, USA
[4] INAF Osservatorio Astronomico di Roma, Via Frascati 33, 00078 Monte Porzio Catone (RM), Italy
[5] Space Science Data Center, Agenzia Spaziale Italiana, Via del Politecnico snc, 00133 Roma, Italy
[6] Center for Astrophysics | Harvard & Smithsonian, 60 Garden Street, Cambridge, MA 02138 USA
[7] INAF, Istituto di Astrofisica e Planetologia Spaziali, Via Fosso del Cavaliere, 100 - I-00133 Rome, Italy
[8] ASI – Agenzia Spaziale Italiana, Via del Politecnico snc, 00133 Roma, Italy
[9] Instituto de Astrofísica de Andalucía, IAA-CSIC, Glorieta de la Astronomía s/n, 18008 Granada, Spain
[10] Max-Planck-Institut für Physik, D-85748 Garching, Germany
[11] Science and Technology Institute, Universities Space Research Association, Huntsville, AL 35805, USA
[12] Physics Department and McDonnell Center for the Space Sciences, Washington University in St. Louis, MO, 63130, USA
[13] Université Paris Cité, CNRS, Astroparticule et Cosmologie, F-75013 Paris, France
[14] Institute for Astrophysical Research, Boston University, 725 Commonwealth Avenue, Boston, MA 02215, USA
[15] St. Petersburg State University, 7/9, Universitetskaya nab., 199034 St. Petersburg, Russia
[16] Department of Physics and Astronomy, 20014 University of Turku, Finland
[17] Finnish Centre for Astronomy with ESO, 20014 University of Turku, Finland
[18] Université de Strasbourg, CNRS, Observatoire Astronomique de Strasbourg, UMR 7550, 67000 Strasbourg, France
[19] Instituto de Radioastronomía Millimétrica, Avenida Divina Pastora, 7, Local 20, E-18012 Granada, Spain
[20] INAF Osservatorio Astronomico di Brera, Via E. Bianchi 46, 23807 Merate (LC), Italy
[21] Interdisziplinäres Zentrum für wissenschaftliches Rechnen (IWR), Ruprecht-Karls-Universität Heidelberg, Im Neuenheimer Feld 205, 69120, Heidelberg, Germany
[22] Max-Planck-Institut für Radioastronomie, Auf dem Hügel 69, D-53121 Bonn, Germany
[23] Mullard Space Science Laboratory, University College London, Holmbury St Mary, Dorking, Surrey RH5 6NT, UK
[24] Istituto Nazionale di Fisica Nucleare, Sezione di Padova, 35131 Padova, Italy
[25] Crimean Astrophysical Observatory RAS, P/O Nauchny, 298409, Crimea
[26] Pulkovo Observatory, St.Petersburg, 196140, Russia
[27] Astrophysics Research Institute, Liverpool John Moores University, Liverpool Science Park IC2, 146 Brownlow Hill, Liverpool, UK
[28] Institute of Astronomy and NAO, Bulgarian Academy of Sciences, 1784 Sofia, Bulgaria
[29] Department of Physics, Graduate School of Advanced Science and Engineering, Hiroshima University Kagamiyama, 1-3-1 Higashi-Hiroshima, Hiroshima 739-8526, Japan
[30] Institute of Integrated Research, Institute of Science Tokyo, 2-12-1 Ookayama, Meguro-ku, Tokyo 152-8550, Japan
[31] Hiroshima Astrophysical Science Center, Hiroshima University 1-3-1 Kagamiyama, Higashi-Hiroshima, Hiroshima 739-8526, Japan
[32] Core Research for Energetic Universe (Core-U), Hiroshima University, 1-3-1 Kagamiyama, Higashi-Hiroshima, Hiroshima 739-8526, Japan
[33] Planetary Exploration Research Center, Chiba Institute of Technology 2-17-1 Tsudanuma, Narashino, Chiba 275-0016, Japan
[34] Graduate School of Sciences, Tohoku University, Aoba-ku, 980-8578 Sendai, Japan
[35] Korea Astronomy and Space Science Institute, 776 Daedeok-daero, Yuseong-gu, Daejeon 34055, Korea
[36] University of Science and Technology, Korea, 217 Gajeong-ro, Yuseong-gu, Daejeon 34113, Korea
[37] Section of Astrophysics, Astronomy & Mechanics, Department of Physics, National and Kapodistrian University of Athens, Panepistimiopolis Zografos 15784, Greece
[38] GFZ Helmholtz Centre for Geosciences, Telegrafenberg, 14476, Potsdam, Germany
[39] Julius-Maximilians-Universität Würzburg, Institut für Theoretische Physik und Astrophysik, Lehrstuhl für Astronomie, Emil-Fischer-Straße 31, 97074 Würzburg, Germany
[40] Dr. Karl-Remeis Sternwarte and Erlangen Centre for Astroparticle Physics, Friedrich-Alexander Universität Erlangen-Nürnberg, Sternwartstr. 7, 96049 Bamberg, Germany

Appendix A: Sample and observations

Table A.1. Detailed description of the sample of HSP sources (first 6 sources) and the LSP sources (last 10 sources).

Source	Time span of observations	Number of observations	Jet direction [deg]	PD [%]	PA [deg]
1ES 0229+200	Jan 15 - Feb 1, 2023	1	70.0 ± 8.5	17.9 ± 2.8	25.0 ± 4.6
Mrk 421	May 4, 2022 - Dec 22, 2023	4	Variable	12.0 ± 5.7	-2.14 ± 31.5
PG 1553+113	Feb 1 - 9, 2023	1	90.0 ± 8.5	10.1 ± 2.3	86.0 ± 8.0
Mrk 501	Mar 8, 2022 - Jan 5, 2025	8	-60.0 ± 12.0	10.8 ± 3.8	-50.7 ± 12.6
1ES 1959+650	May 3, 2022 - Aug 19, 2023	4	Variable	8.7 ± 1.9	-16.65 ± 47.2
PKS 2155-304	Oct 27 - Nov 7, 2023	1	-45.0 ± 8.5	23.0 ± 7.7	-52.6 ± 2.9
PKS 0420-01	Oct 28,2013 - Nov 4, 2015	10	-61.8 ± 19.4	12.4 ± 6.3	-8.55 ± 52.3
4C 71.07	Jun 24, 2013 - Nov 23, 2015	10	40.5 ± 11.8	2.7 ± 4.2	-6.15 ± 15.5
PKS 1510-089	May 30, 2013 - Jun 30, 2017	85	-26.6 ± 20.5	4.9 ± 4.0	5.9 ± 51.7
4C 38.41	May 31, 2013 - Sep 5, 2016	93	-57.0 ± 16.1	6.6 ± 4.3	11.7 ± 43.0
3C 345	Jun 8, 2013 - Sep 18, 2017	36	81.8 ± 14.0	4.9 ± 2.7	52.5 ± 30.0
4C 09.57	May 31, 2013 - Sep 5, 2016	94	-2.3 ± 17.0	10.1 ± 5.6	-20.4 ± 45.6
BL Lac	Jun 19, 2913 - Dec 1, 2023	1603	9.2 ± 7.2	10.7 ± 9.1	32.2 ± 37.6
3C 446	Jun 23, 2013 - Aug 16, 2015	10	-54.1 ± 19.0	15.3 ± 6.2	-25.4 ± 26.4
4C 11.69	Jun 23, 2013 - Oct 20, 2017	97	-50.3 ± 13.3	4.4 ± 3.6	6.4 ± 39.8
3C 454.3	Jun 21, 2013 - Jul 2, 2023	209	-81.0 ± 19.5	4.3 ± 3.4	-26.3 ± 45.5

Notes. The column "Time span of observations" indicates the dates of the first and the last observation. Note that the observations do not cover the entire period indicated in the column, but rather intervals within that time span. The column "Number of observations" indicates the number of measurements taken into account for each source. The columns "PD" and "PA" refer to the median values over all the observations taken into account in this work, with their errors. The jet directions defined as "Variable" indicate that different values have been used for different observations (see Table A.2 for details). Both jet direction and angle are defined between [-90°, 90°].

Table A.2. IXPE observations of the HSP sample taken into account in this work, together with the previous publications used for this analysis.

Source	obsID	Dates	Jet direction	Polarisation properties
Mrk 421	01003701	May 4-6, 2022	Weaver et al. (2022)	Di Gesu et al. (2022)
	01003801	Jun 4-6, 2022		Di Gesu et al. (2023)
	02004401	Dec 6-8, 2022		Kim et al. (2024)
	02008199	Dec 6-22, 2023	Maksym et al. (2024)	Maksym et al. (2024)
Mrk 501	01004501	Mar 8-10, 2022	Weaver et al. (2022)	Chen et al. (2024)
	01004601	Mar 27-29, 2022		
	01004701	Jul 9-12, 2022		
	02004601	Feb 12-14, 2023		
	02004501*	Mar 19-21, 2023		
	02004701	Apr 16-18, 2023		
	03008801	Apr 8-10, 2024		This work
	03008901	Jul 7-9, 2024		This work
	03009001	Aug 10-12, 2024		This work
	03009101*	Jan 3-5, 2025		This work
1ES 1959+650	01006201	May 3-4, 2022	Errando et al. (2024)	Errando et al. (2024)
	01006001⋆	Jun 9-12, 2022		
	02004801	Oct 28-31, 2022	Pacciani et al. (2025)	Pacciani et al. (2025)
	02250801	Aug 14-19, 2023		
1ES 0229+200	01006499	Jan 15-Feb 1, 2023	Piner & Edwards (2018)	Ehlert et al. (2023)
PG 1553+113	02004999	Feb 1-9, 2023	90° †	Middei et al. (2023b)
PKS 2155−304	02005601	Oct 27-Nov 7, 2023	Kouch et al. (2024)	Kouch et al. (2024)

Notes. The columns "Jet direction" and "Polarisation properties" refer to the works from which the values of the jet direction and the average PD, PA and errors were taken. The observations reported with * were not taken into account for this analysis, as they were 3σ upper limits on PD and not detections. The observation reported with ⋆ was originally divided into four equal time bins, of which we only used the third, as the other three were upper limits. The value reported with † comes from private communications. No error was indicated, therefore the value used was the average over the errors of the other jet measurements. For the new IXPE observations of Mrk 501 (indicated with "This work"), see Table B.1.

Appendix B: New multiwavelength observations of Mrk 501

Table B.1. Polarisation properties of Mrk 501 measured by IXPE during the new observations (2024, 2025) carried out during Cycle 1.

obsID	Start time [MJD]	End time [MJD]	PD [%]	PD error [%]	PA [deg]	PA error [deg]
03008801	60408.108	60410.176	17.4	2.8	124.7	4.6
03008901	60498.836	60500.912	11.7	2.4	135.5	6.0
03009001	60530.194	60534.295	11.2	2.9	137.2	7.5
03009101	60678.163	60680.194	≤14.9	-	-	-

Notes. Start and end time are reported, together with the median polarisation degree and its error, as well as the median polarisation angle and its error. The last observation was not a detection, but a 3σ upper limit, and therefore has no measurement on the PA and it was not included in the analysis.

Table B.2. Median values of the polarisation properties measured during multiwavelength observations of Mrk 501, simultaneous to the new IXPE observations.

obsID	Band	PD [%]	PD error [%]	PA [deg]	PA error [deg]
03008801	4 GHz	1.8	0.2	175.3	2.6
	10 GHz	3.2	1.6	166.9	3.8
	15 GHz	1.4	0.2	161.6	2.5
	R	1.8	0.2	175.3	2.6
03008901	R	4.8	1.2	126.9	5.5
	V	2.8	0.3	121	3.9
	B	2.5	0.5	127.4	4.8
03009001	225 GHz	2.6	0.7	159.1	5.7
	R	6.7	1.6	125.5	5
	V	3.4	0.1	124.2	1.0
	B	4.4	0.2	124.9	0.5
03009101	R	3.6	0.2	125.5	1.3

Notes. Only the bands that had available measurements are reported.